Editors' Suggestion

Probing Multipolar Order in the Candidate Altermagnet MnF_2 through the Elastocaloric Effect under Strain

Rahel Ohlendorf,[1,2,*] Luca Buiarelli,[3] Hilary M. L. Noad,[1] Andrew P. Mackenzie,[1,4] Rafael M. Fernandes,[5,6] Turan Birol,[3] Jörg Schmalian,[7,8] and Elena Gati[1,2,9,†]

[1]*Max Planck Institute for Chemical Physics of Solids, 01187 Dresden, Germany*
[2]*Institut für Festkörper- und Materialphysik, Technische Universität Dresden, 01062 Dresden, Germany*
[3]*Department of Chemical Engineering and Materials Science, University of Minnesota, Minneapolis, Minnesota 55455, USA*
[4]*Scottish Universities Physics Alliance, School of Physics and Astronomy, University of St Andrews, St. Andrews KY16 9SS, United Kingdom*
[5]*Department of Physics, The Grainger College of Engineering, University of Illinois Urbana-Champaign, Urbana, Illinois 61801, USA*
[6]*Anthony J. Leggett Institute for Condensed Matter Theory, The Grainger College of Engineering, University of Illinois Urbana-Champaign, Urbana, Illinois 61801, USA*
[7]*Institute for Theory of Condensed Matter, Karlsruhe Institute of Technology, 76131 Karlsruhe, Germany*
[8]*Institute for Quantum Materials and Technologies, Karlsruhe Institute of Technology, 76126 Karlsruhe, Germany*
[9]*Institute of Physics, Goethe University, 60438 Frankfurt/Main, Germany*

(Received 27 January 2026; revised 13 May 2026; accepted 16 June 2026; published 28 July 2026)

Altermagnets break a combination of time-reversal and rotational symmetries without generating a net magnetization. As such, the order parameter of d-wave altermagnets has the same symmetry as magnetic multipoles and couples to the product of a magnetic field and uniaxial strain. We combine elastocaloric experiments, free-energy modeling, and first-principles calculations on MnF_2 to establish a thermodynamic probe of the predicted finite-temperature altermagnetic critical point. These results pave the way to explore altermagnetic quantum criticality in d-wave materials and beyond.

DOI: 10.1103/svrz-315w

Introduction—Symmetry analysis is a cornerstone of condensed-matter physics, providing a rigorous framework for identifying broken-symmetry states. In the context of collinear magnetism, a recent classification based on spin groups has revealed a rich variety of magnetic orders that extend far beyond conventional dipolar ferro- and antiferromagnets. Among these, so-called altermagnets (AMs) [1–3] have garnered significant attention recently due to their unique electronic structure, characterized by an alternating spin polarization [4,5] of the energy bands combined in certain cases with zero net magnetization [6]. This property opens pathways toward novel functionalities in metallic spintronic devices [2,7].

The distinctive features of AMs arise from their compensated magnetic structures, which preserve combinations of time-reversal and rotational point-group symmetries. Because the relevant symmetry constraints involve operations both in spin space and in real space [8,9], AM order parameters can be interpreted in terms of higher-rank multipole orders [6,10–14] instead of a conventional dipole order [15].

The symmetries of an ordered phase impose strict constraints on its allowed response functions. While recent studies have focused on spectroscopic and transport signatures of the unconventional symmetry breaking in AMs [16–18], thermodynamic characterization remains less explored. However, such measurements offer fundamental insights, since the application of a conjugate field $\hat{h}$—an external perturbation that transforms like the order parameter—causes a distinct thermodynamic response that is a direct consequence of the broken symmetry in the ordered state. One key prediction is that a sharp phase transition at $\hat{h} = 0$ and temperature T_c becomes a crossover at finite $\hat{h}$, with the associated crossover temperature T^* obeying the scaling relation

$$T^* - T_c \propto \hat{h}^{1/(\beta\delta)}, \tag{1}$$

where β and δ are the critical exponents of the transition that determine, as usual, the change of the order parameter with temperature and conjugate field, respectively. Moreover, near the critical point at $(\hat{h} = 0, T_c)$, the entropy

*Contact author: Rahel.Ohlendorf@cpfs.mpg.de
†Contact author: e.gati@physik.uni-frankfurt.de

is expected to peak and to decrease as one applies the external conjugate field $\hat{h}$.

With the exception of ferromagnets and nematics, where $\hat{h}$ corresponds to a uniform magnetic field and uniaxial strain, the physical realization of a conjugate field is often challenging, even if the magnetic order is collinear. For instance, in a two-sublattice antiferromagnet that breaks translational symmetry, $\hat{h}$ is a staggered magnetic field that alternates between the sublattices. A distinctive feature of AMs with a d-wave component (or, equivalently, a ferroic order of emergent magnetic octupole moments) is that piezomagnetism [19–21] allows $\hat{h}$ to be realized through a combination of magnetic field and strain [11,22–26], enabling thermodynamic measurements to reveal the nature of the broken symmetry.

In this Letter, we experimentally verify such key thermodynamic predictions resulting from the symmetry breaking in a d-wave AM. This type of AM is proposed to exist in rutile insulating compounds [2,10,27–29], such as MnF_2 and CoF_2, which have d_{xy}-wave symmetry, and metallic systems [30,31]. Based on the symmetry analysis, the rutile systems exhibit an emergent ferroic time-reversal symmetry breaking octupolar order [10] [see Figs. 1(a) and 1(b)]. These symmetry considerations allow us to identify the relevant conjugate field $\hat{h}$ as a combination of a magnetic field along the z axis, $\mu_0 H_z$, and a symmetry-breaking shear strain ε_{xy}, i.e.,

$$\hat{h} = \mu_B \varepsilon_{xy} \mu_0 H_z. \tag{2}$$

As a method of choice to explore the thermodynamics of AMs [11,24,32] experimentally, we focus here on the elastocaloric effect (ECE)—the adiabatic temperature change induced by strain:

$$\eta_{ij} = \left(\frac{\partial T}{\partial \varepsilon_{ij}}\right)_S = -\frac{T}{C_{\varepsilon_{ij}}}\left(\frac{\partial S}{\partial \varepsilon_{ij}}\right)_T, \tag{3}$$

which is thermodynamically related to the temperature (T) and strain (ε_{ij}) derivative of the entropy (S). $C_{\varepsilon_{ij}} = -T(\partial S/\partial T)_{\varepsilon_{ij}}$ is the specific heat at constant strain. The ECE has recently emerged as a highly sensitive probe of symmetry breaking in quantum materials, enabled by recent advances in *in situ*-tunable uniaxial pressure cells [33–40]. Despite theoretical results showing the connection between ECE and the AM susceptibility [26,41], the ECE has not yet been experimentally explored in the context of the multipolar order of AMs.

Here, we establish the sensitivity of the ECE to AM symmetries through experiments on MnF_2 combined with symmetry analysis, free energy modeling, and density functional theory (DFT). MnF_2 is particularly well suited for our study owing to its well-characterized magnetic order below the accessible transition temperature $T_c^{(0)} = 67.5$ K [28,42,43], its known piezomagnetism [44,45] reflecting the underlying spatial and spin symmetries, prior evidence of aspherical magnetization density around Mn ions [46], and the recent observation of AM magnon splitting [47].

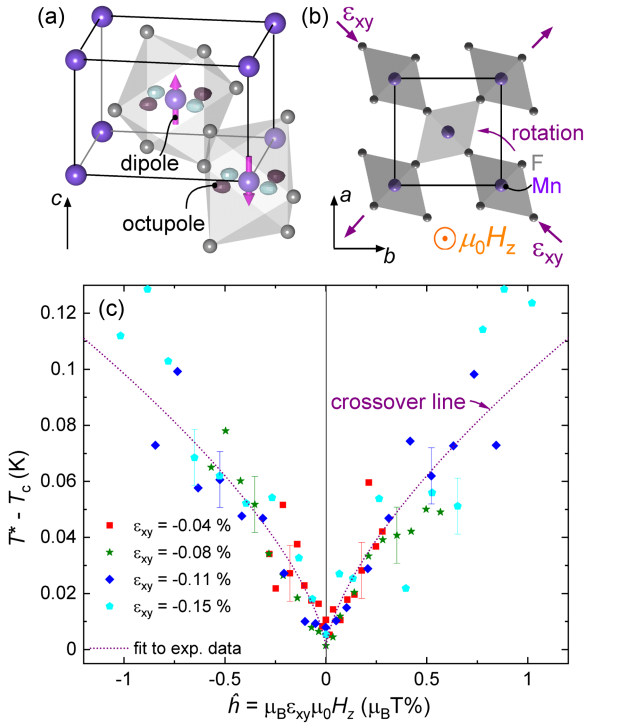

FIG. 1. (a) Emergent ferro-octupolar order [10,14] of the AM candidate MnF_2. The pink arrows depict the antiferromagnetic ordering of dipoles, whereas the ferroically ordered octupoles are depicted in purple and cyan. (b) A top view of the crystal structure. The F ions (gray circles) create an octahedral environment around the Mn atoms (purple circles); as a result, the two Mn sublattice sites are related by a nonsymmorphic symmetry involving a 90° rotation and a half-translation. A strain ε_{xy} will break this rotational symmetry. The conjugate field to the AM order, $\hat{h}$, is composed of ε_{xy} and a magnetic field along the c axis, $\mu_0 H_z$. (c) Experimentally determined crossover lines $T^* - T_c$ of MnF_2 as a function of conjugate field $\hat{h} = \mu_B \mu_0 H_z \varepsilon_{xy}$. The experimental data, extracted from the data in Fig. 2 and in End Matter, follow the expectation for an AM critical point at $\mu_B \mu_0 H_z \varepsilon_{xy} = 0$. The data are well described by a fit to Eq. (5) with the mean-field exponent $1/(\beta\delta) = 2/3$. For clarity, error bars are shown only for representative data points.

Our key result is the experimental identification of the predicted crossover lines in MnF_2 [see Fig. 1(c)]. We complement this by identifying signatures of entropy accumulation in the vicinity of the transition temperature. Furthermore, we show through DFT calculations that the observed thermodynamic response can be microscopically explained by a weakly spin-orbit-coupled AM insulator with a small degree of off-stoichiometry. Our results provide a road map for future thermodynamic investigations of strain-tuned AMs, in particular, for experimental explorations of AM quantum criticality [26,41] in both insulators and metals.

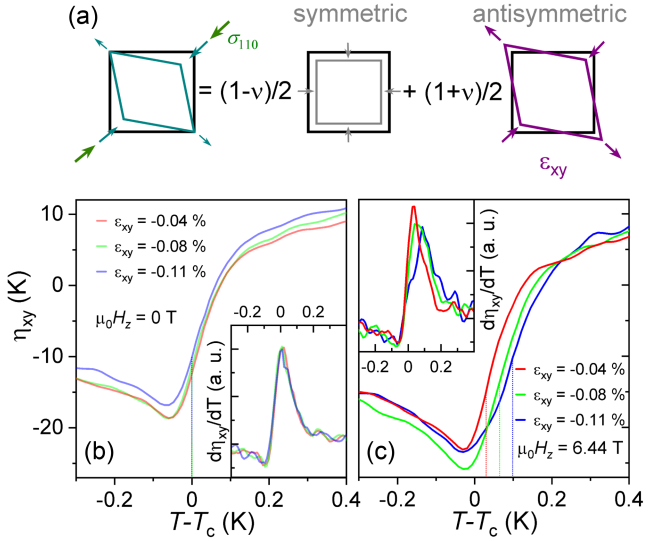

FIG. 2. (a) The application of a uniaxial stress along the [110] direction, σ_{110}, leads to an induced strain that can be described by the superposition of a symmetric strain and an antisymmetric strain. The latter is denoted by ε_{xy}, and ν is the Poisson ratio. (b), (c) ECE data η_{xy} on MnF_2 as a function of the relative temperature $T - T_c$. T_c is the transition temperature including non-AM shifts in strain and field (see the text). While for $\mu_0 H_z = 0$ T (b) the ECE features occur at the same temperature (see dotted lines, representing the point of steepest slope), they move to higher temperature with higher compression for 6.44 T (c), as expected for a system with AM order. The insets in (b) and (c) show the temperature derivatives of the ECE data in the respective plots. The maxima of the derivatives mark the points of steepest slope in the ECE data.

Results and discussion—In order to induce a ε_{xy} strain experimentally, we apply a uniaxial stress along the crystallographic [110] direction, σ_{110} [see Fig. 2(a)]. Such a stress generates both the symmetry-breaking ε_{xy} component and a fully symmetric component $1/2(\varepsilon_{xx} + \varepsilon_{yy})$. Importantly, for any generic symmetry of the order parameter, the symmetric strain can always shift $T_c^{(0)}$ linearly, as can $(\mu_0 H_z)^2$ (see Supplemental Material [48], Sec. C2). Thus, the extended AM free energy, including all terms relevant for experiments under σ_{110}, reads as [22,26,41]

$$f = \frac{k_B}{2}(T - T_c)\Phi^2 + \frac{u}{4}\Phi^4 - \lambda \hat{h}\Phi \tag{4}$$

with $T_c = T_c^{(0)} + a_0 \frac{1}{2}(\varepsilon_{xx} + \varepsilon_{yy}) + a_2(\mu_0 H_z)^2$. $T_c^{(0)}$ is the transition temperature at zero strain and magnetic field, and Φ is the AM order parameter, which couples to its conjugate field with a coupling constant λ (note that per definition λ is dimensionless here). Since $(\varepsilon_{xx} + \varepsilon_{yy}) \propto \sigma_{110} \propto \varepsilon_{xy}$ (see Supplemental Material, Sec. C2 [48]), we can analyze our results in terms of any of these three variables, with the understanding that the physical external control parameter is σ_{110}. Since our primary interest is on the altermagnetic term, hereafter we choose to express our results in terms of ε_{xy}. Consequently, when T_c is plotted as a function of ε_{xy}, it also has a linear contribution, resulting in the following equation for T_c: $T_c = T_c^{(0)} + a_1 \varepsilon_{xy} + a_2(\mu_0 H_z)^2$. We obtain (see Supplemental Material, Sec. C1 [48])

$$T^* = T_c + T_c \left(\frac{\lambda \hat{h}}{k_B T_c}\right)^{1/(\beta\delta)}, \tag{5}$$

which is Eq. (1) given above.

Figures 2(b) and 2(c) show thermodynamic ECE data η_{xy}, which reveal distinct features that we trace as a function of relative temperature $T - T_c$, for $\mu_0 H_z = 0$ T (b) and 6.44 T (c) [using $T_c^{(0)} = 67.467(3)$ K, $a_2 = -0.015\,85(14)$ K/T^2, and $a_1 = -59(3)$ K, determined from a global fit; see Supplemental Material Sec. D4 [48]]. The characteristic temperatures T_c (at $\hat{h} = 0$) and $T^\star$ (at $\hat{h} \neq 0$) are defined by the point of steepest slope in $\eta_{xy}(T)$, which corresponds to a maximum in the derivative of $\eta_{xy}(T)$ (see insets). In each panel, we show $\eta_{xy}(T - T_c)$ at three different compressive ε_{xy} values. In zero field, the steplike feature appears at $T = T_c$ for all ε_{xy}. Under a fixed finite field, however, the feature shifts to higher T with increasing ε_{xy} [dotted lines in Fig. 2(c)], indicating a combined action of ε_{xy} and $\mu_0 H_z$.

The result of $T^\star - T_c$ as a function of $\hat{h}$, compiled from all datasets that are shown in Figs. 5 and 6 in End Matter, is presented in Fig. 1(c). Importantly, the data exhibit a sharp kink at $\hat{h} = 0$, are symmetric around that point, and collapse for all different ε_{xy} onto a single curve within the experimental resolution. This behavior matches the expectation for the crossover lines from the analysis of the AM free energy. Fitting the data in Fig. 1(c) with Eq. (5) using the mean-field critical exponent of $1/(\beta\delta) = 2/3$ yields $\lambda = 0.56(5)$ [while a fit using the 3D Ising critical exponent of $1/(\beta\delta) \approx 0.64$ yields $\lambda = 0.35(5)$; see Supplemental Material Sec. C1 [48]].

We further support the thermodynamic evidence for AM symmetries of Φ by identifying AM signatures directly in the magnitude of η_{xy}. In Fig. 3, we compare the experimental $\eta_{xy}(T)$ at fixed strain $\varepsilon_{xy} = -0.11\%$ and varying $\mu_0 H_z$ with simulations based on the mean-field free energy Eq. (4), with a_1, a_2, and λ as above. Two distinct contributions to $\eta_{xy}(T)$ can be identified. First, in zero field, both experiment and theory show a jumplike change at T_c, consistent with the Ehrenfest relation $\Delta\eta_{xy} \propto dT_c/d\varepsilon_{xy} = a_1$ [see Eq. (A1)], i.e., a field-independent, non-AM contribution to $\eta_{xy}(T)$, since it does not depend on the AM coupling λ. Second, for finite fields, we find that both experiment and simulations show a stronger negative response upon approaching T^* from below (note that the general suppression of T^* is a consequence of the a_2 parameter). On a quantitative level, there is a good

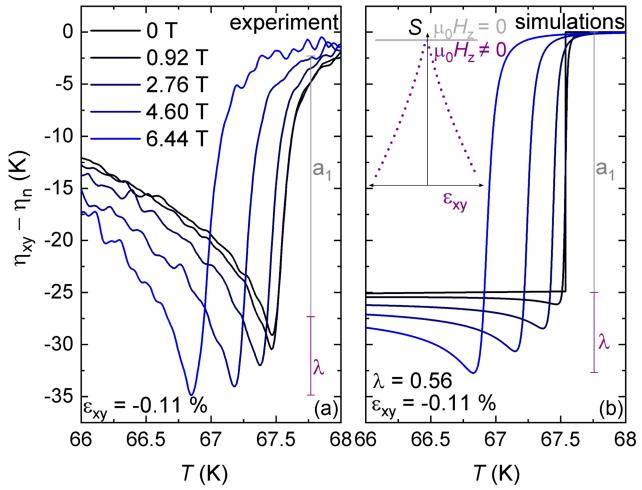

FIG. 3. Comparison of (a) experimental $\eta_{xy} - \eta_n$ (with η_n the high-temperature background; see End Matter) of MnF_2 as a function of T at a fixed strain of $\varepsilon_{xy} = -0.11\%$ and different fields up to 6.44 T with (b) mean-field simulations for η_{xy}, based on the free energy Eq. (4). The contributions to η_{xy} due to a_1 and λ are marked by vertical bars. The AM contribution associated with λ leads to a negative change in η_{xy} under finite fields, as the entropy S grows toward a maximum at zero strain (see the inset).

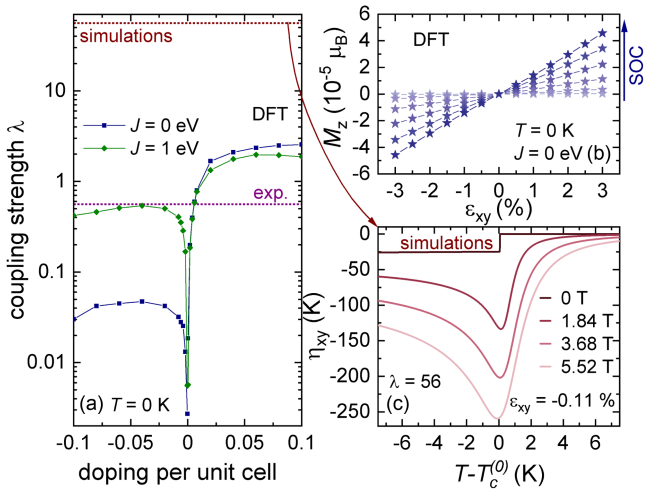

FIG. 4. (a) Magnitude of λ per unit cell as a function of additional carrier concentration from DFT calculations. Introduction of ~0.001 holes per unit cell ($\sim 10^{19}$ cm^{-3}) in the DFT calculations provides agreement with the experimental observation (dotted pink line) for reasonable values of the Hund's coupling J. (b) Net magnetic moment M_z per unit cell of MnF_2 as a function of ϵ_{xy} shear strain for different magnitudes of SOC calculated from DFT. Even though the spin group analysis allows the M_z PZM response to be finite, our calculations indicate that the corresponding component λ is suppressed at zero temperature because of the large band gap when SOC is not taken into account. (c) Simulations of η_{xy} vs $T - T_c^{(0)}$ for a higher value of λ [dotted red line in (a)], which may be realized in other materials with metallic character or larger SOC [see (b) and End Matter]. The predicted η_{xy} values should be readily observable in experiments over a wider temperature range, enabling the direct measurement of the AM susceptibility.

agreement between simulations and experiment: The minimum of η_{xy} decreases in both by ≈6–8 K when $\mu_0 H_z$ increases from 0 to 6.44 T.

This change in ECE magnitude can be attributed to the AM term in the free energy, i.e., is a consequence of λ. The change in η_{xy} with $\mu_0 H_z$ at fixed ε_{xy} directly reflects the entropy accumulation at the critical point ($\varepsilon_{xy}\mu_0 H_z = 0$, T_c). For finite $\mu_0 H_z$, the critical endpoint becomes strain controlled, enforcing a symmetric entropy landscape around the maximum at $\varepsilon_{xy} = 0$ (see the inset in Fig. 3). Consequently, the ECE contribution is negative for compressive strain and grows with increasing $\mu_0 H_z$, as the field effectively renders λ field dependent. Importantly, the ECE magnitude related to the AM term λ can reach experimentally resolvable magnitudes even for moderate λ, since the Grüneisen parameter $\Gamma_{xy} = \eta_{xy}/T$ is expected to nearly diverge [67] at a finite-T critical endpoint due to the entropy accumulation.

Next, to gain insight into the microscopic origin and magnitude of λ, we link it to the piezomagnetic (PZM) response obtained from first-principles DFT calculations [see Figs. 4(a) and 4(b)]. Spin-group analysis allows only one PZM response to be nonzero without spin-orbit coupling, given by $M_z = -\partial f/\partial B_z = \lambda \mu_B \Phi \varepsilon_{xy}$ (see End Matter, Sec. B). Using that by convention $\Phi \approx 1$ deep in the ordered state, we estimate λ from the calculated PZM response.

In the DFT calculations (see Supplemental Material, Sec. C5 [48]), the AM phase of MnF_2 with magnetic moments parallel to the crystallographic c axis is considered, and self-consistent calculations are repeated for varying magnitudes of ϵ_{xy} strain to obtain the magnitude of the induced unit cell magnetic dipole moment along the c axis. Interestingly, while spin-group analysis predicts that PZM induced by ε_{xy} [see Fig. 4(b)] should be allowed in the AM phase without spin-orbit coupling (SOC) [68], DFT calculations show that it is strongly suppressed in the absence of SOC at zero temperature. This can be explained by the fact that MnF_2 is an insulator, and it is not possible to induce a magnetic moment in fully occupied bands without exciting electrons across the band gap [14,25]. This is supported by the observation that increasing electronic temperature enhances the PZM coefficient in DFT [see End Matter, Fig. 7(a)].

However, our DFT calculations for pristine MnF_2 with finite SOC consistently underestimate the experimentally observed λ, and introducing reasonable values of the Hubbard U or Hund's coupling J does not alter this result [see Fig. 7(b)]. A potential explanation for the discrepancy between calculations and experiment could be finite-temperature effects. It was recently proposed that thermally excited magnons also contribute to λ as T_c is approached

from below in insulating antiferromagnets [24,25]. However, in this case a strong temperature dependence of λ is expected, which was not observed in an earlier measurement of the PZM in MnF_2 [69].

In the following, we show that another way to reconcile this disagreement is to take into account the presence of additional electrons or holes in the system. Although our samples are of high quality, we cannot fully exclude the presence of defects or slight off-stoichiometry. For example, even a one part in 10^3 off-stoichiometry leads to $\sim 10^{19}$ cm^{-3} electrons or holes, which is much higher than obtained through thermal excitations across the gap (note that, for piezomagnetism, what matters is whether the additional charges are spin polarizable, not whether they are itinerant; in insulating MnF_2, off-stoichiometry likely results in localized charges). In order to simulate this effect, we repeated our DFT calculations with added electrons or holes and extracted λ [see Fig. 4(a)]. Both electrons and holes initially enhance λ by orders of magnitude before it shows a saturationlike behavior. Even though the sign of the coefficient is the same for either type of doping, there is strong electron-hole asymmetry in the size of response, which is particularly pronounced at $J = 0$. This can be understood by considering which sites the carriers occupy in the DFT calculations [see Fig. 7(c)]. Doped electrons occupy the widest t_{2g} bands formed by d orbitals elongated along the Mn chains along the c axis. The spin density is nonzero on both opposite spin Mn ions, and, hence, their net magnetic moment is canceled to a large extent. Doped holes, on the other hand, occupy the narrower e_g bands on top of the valence band, and the DFT results indicate that most of them occupy only one of the Mn ions' orbitals under strain, hence giving rise to an enhanced net magnetic moment. Introducing additional on-site Hund's coupling J reduces this electron-hole asymmetry but does not completely eliminate it. In either case, we estimate that about 0.001 holes per Mn is sufficient to obtain results that agree with the experimental observation. Note, however, that the magnitude of this effect is meaningful only as an order of magnitude because of the tendencies of DFT to overestimate magnetic order in partially filled orbitals and to underestimate electron localization.

These insights highlight that even very small deviations from stoichiometry can significantly affect the magnitude of λ in AM insulators. For MnF_2, where only a single prior measurement exists for this combination of strain and field [45] (see End Matter, Sec. B), this sensitivity likely rationalizes remaining discrepancies of earlier studies with our results, in addition to experimental factors such as background signals.

Summary and outlook—In this Letter, we establish a direct thermodynamic measurement of the octupolar symmetry of the AM order parameter of MnF_2. By exploiting the elastocaloric effect as an exceptionally sensitive probe of the strain and field dependence of the AM free energy, we determine the cusp-shaped dependence of the crossover scale T^* at the AM phase transition as a function of the field conjugate to the AM order parameter. In this way, the underlying PZM makes it possible to observe the otherwise hidden AM order parameter experimentally, even in systems, such as MnF_2, where the PZM coupling is relatively weak.

Taken together, the present results open the way to applying this novel ECE methodology to other AM candidates with varying λ. In AMs with a 2 orders of magnitude larger λ, substantial ECE signatures at finite $\hat{h}$—of the type shown in Fig. 4(c)—should emerge. In this case, therefore, ECE measurements should not only enable measurements of the crossover lines and of the entropy accumulation close to T_c, but should also allow the determination of the AM susceptibility for $T \gg T_c$ [26,38,41]. Since we suggest from our DFT results that λ can be orders of magnitude larger in AM metals, where a band gap is absent, ECE measurements should be particularly powerful in metallic d-wave AMs.

Importantly, the finite SOC in real materials will also extend the reach of ECE measurements beyond d-wave octupolar AMs. This is because in higher-order g-wave AMs such as hematite [70] and MnTe and CrSb, even though spin-group symmetries forbid intrinsic octupole moments, SOC necessarily induce them [6,13,14], thereby leading to PZM responses [71,72].

Beyond uncovering the thermodynamic signatures of unconventional symmetry breaking of multipolar order in AMs, the prediction of resolvable elastocaloric effects offers a compelling route to access AM fluctuations near putative quantum critical points [26,41], akin to studies of nematic quantum criticality in the pnictides [73]. This positions the ECE approach as a powerful probe of, e.g., superconductivity [74] induced by AM (i.e., multipolar) quantum critical fluctuations [75].

Acknowledgments—We thank Bernd Wolf and Wolf Aßmus for kindly providing the MnF_2 crystal and Jan Priessnitz, Libor Smejkal, and Charles R. W. Steward for useful discussions. Financial support from the Max Planck Society (R. O., H. M. L. N., A. P. M., and E. G.) is gratefully acknowledged. In addition, R. O., H. M. L. N., A. P. M., J. S., and E. G. gratefully acknowledge the funding through the Deutsche Forschungsgemeinschaft (DFG, German Research Foundation) through Grant No. TRR 288-422213477 Elasto-Q-Mat (Projects No. A10, No. A13, and No. B01). Research in Dresden benefits from the environment provided by the DFG Cluster of Excellence ctd.qmat (EXC 2147, Project ID No. 390858490). R. M. F. was supported by the Air Force Office of Scientific Research under Award No. FA9550-21-1-0423. R. M. F. also acknowledges a Mercator Fellowship from the German Research Foundation (DFG) through Grant No. TRR 288-422213477 Elasto-Q-Mat. L. B. and T. B. were supported by the National Science Foundation CAREER Grant

No. DMR-2046020 and also partially supported by the National Science Foundation through the University of Minnesota MRSEC under Award No. DMR-2011401.

Data availability—The data that support the findings of this article are openly available [76].

[1] L. Šmejkal, J. Sinova, and T. Jungwirth, Phys. Rev. X **12**, 031042 (2022).
[2] L. Šmejkal, J. Sinova, and T. Jungwirth, Phys. Rev. X **12**, 040501 (2022).
[3] T. Jungwirth, R. M. Fernandes, E. Fradkin, A. H. MacDonald, J. Sinova, and L. Šmejkal, Newton **1**, 100162 (2025).
[4] L. Šmejkal, R. González-Hernández, T. Jungwirth, and J. Sinova, Sci. Adv. **6**, eaaz8809 (2020).
[5] S. Hayami, Y. Yanagi, and H. Kusunose, J. Phys. Soc. Jpn. **88**, 123702 (2019).
[6] R. M. Fernandes, V. S. de Carvalho, T. Birol, and R. G. Pereira, Phys. Rev. B **109**, 024404 (2024).
[7] T. Jungwirth, J. Sinova, P. Wadley, D. Kriegner, H. Reichlova, F. Krizek, H. Ohno, and L. Smejkal, arXiv:2508.09748.
[8] W. F. Brinkman, R. J. Elliott, and R. E. Peierls, Proc. R. Soc. A **294**, 343 (1966).
[9] D. Litvin and W. Opechowski, Physica (Utrecht) **76**, 538 (1974).
[10] S. Bhowal and N. A. Spaldin, Phys. Rev. X **14**, 011019 (2024).
[11] P. A. McClarty and J. G. Rau, Phys. Rev. Lett. **132**, 176702 (2024).
[12] H. Schiff, P. McClarty, J. G. Rau, and J. Romhányi, Phys. Rev. Res. **7**, 033301 (2025).
[13] R. Jaeschke-Ubiergo, V.-K. Bharadwaj, W. Campos, R. Zarzuela, N. Biniskos, R. M. Fernandes, T. Jungwirth, J. Sinova, and L. Šmejkal, arXiv:2503.10797.
[14] L. Buiarelli, R. M. Fernandes, and T. Birol, Phys. Rev. B **112**, 224442 (2025).
[15] S. Hayami, Y. Yanagi, and H. Kusunose, Phys. Rev. B **102**, 144441 (2020).
[16] T. Jungwirth, J. Sinova, R. M. Fernandes, Q. Liu, H. Watanabe, S. Murakami, S. Nakatsuji, and L. Šmejkal, Nature (London) **649**, 837 (2026).
[17] A. Hariki, A. Dal Din, O. J. Amin, T. Yamaguchi, A. Badura, D. Kriegner, K. W. Edmonds, R. P. Campion, P. Wadley, D. Backes *et al.*, Phys. Rev. Lett. **132**, 176701 (2024).
[18] J. Krempaský, L. Šmejkal, S. W. D'Souza, M. Hajlaoui, G. Springholz, K. Uhlířová, F. Alarab, P. C. Constantinou, V. Strocov, D. Usanov *et al.*, Nature (London) **626**, 517 (2024).
[19] T. Moriya, J. Phys. Chem. Solids **11**, 73 (1959).
[20] I. Dzyaloshinskii, Zhur. Eksptl'. i Teoret. Fiz. **33**, 1454 (1957).
[21] B. Tavger, Sov. Phys. Crystallogr. **3**, 341 (1958).
[22] C. R. W. Steward, R. M. Fernandes, and J. Schmalian, Phys. Rev. B **108**, 144418 (2023).
[23] J.-Y. Li, A.-D. Fan, Y.-K. Wang, Y. Zhang, and S. Li, Appl. Phys. Lett. **125**, 241101 (2024).
[24] K. V. Yershov, V. P. Kravchuk, M. Daghofer, and J. van den Brink, Phys. Rev. B **110**, 144421 (2024).
[25] M. Khodas, S. Mu, I. I. Mazin, and K. D. Belashchenko, Phys. Rev. B **113**, 104422 (2026).
[26] A. R. Chakraborty, J. Schmalian, and R. M. Fernandes, Phys. Rev. B **112**, 035146 (2025).
[27] M. Roig, A. Kreisel, Y. Yu, B. M. Andersen, and D. F. Agterberg, Phys. Rev. B **110**, 144412 (2024).
[28] V. C. Morano, Z. Maesen, S. E. Nikitin, J. Lass, D. G. Mazzone, and O. Zaharko, Phys. Rev. Lett. **134**, 226702 (2025).
[29] D. S. Antonenko, R. M. Fernandes, and Jorn W. F. Venderbos, Phys. Rev. Lett. **134**, 096703 (2025).
[30] B. Jiang, M. Hu, J. Bai, Z. Song, C. Mu, G. Qu, W. Li, W. Zhu, H. Pi, Z. Wei *et al.*, Nat. Phys. **21**, 754 (2025).
[31] Y. Sun, Y. Huang, J. Cheng, S. Zhang, Z. Li, H. Luo, X. Ma, W. Yang, J. Yang, D. Chen, K. Sun, M. Gutmann, S. C. Capelli, F. Shen, J. Hao, L. He, G. Chen, and S. Li, Phys. Rev. B **112**, 184416 (2025).
[32] A. S. Patri, A. Sakai, S. Lee, A. Paramekanti, S. Nakatsuji, and Y. B. Kim, Nat. Commun. **10**, 4092 (2019).
[33] C. W. Hicks, M. E. Barber, S. D. Edkins, D. O. Brodsky, and A. P. Mackenzie, Rev. Sci. Instrum. **85**, 065003 (2014).
[34] M. S. Ikeda, T. Worasaran, J. C. Palmstrom, J. A. W. Straquadine, P. Walmsley, and I. R. Fisher, Phys. Rev. B **98**, 245133 (2018).
[35] Y.-S. Li, M. Garst, J. Schmalian, S. Ghosh, N. Kikugawa, D. A. Sokolov, C. W. Hicks, F. Jerzembeck, M. S. Ikeda, Z. Hu *et al.*, Nature (London) **607**, 276 (2022).
[36] L. Ye, Y. Sun, V. Sunko, J. F. Rodriguez-Nieva, M. S. Ikeda, T. Worasaran, M. E. Sorensen, M. D. Bachmann, J. Orenstein, and I. R. Fisher, Proc. Natl. Acad. Sci. U.S.A. **120**, e2302800120 (2023).
[37] E. Gati, B. Schmidt, S. L. Bud'ko, A. P. Mackenzie, and P. C. Canfield, npj Quantum Mater. **8**, 69 (2023).
[38] L. Ye, M. E. Sorensen, M. D. Bachmann, and I. R. Fisher, Nat. Commun. **15**, 7005 (2024).
[39] Z. Liu, Y. Shi, Q. Jiang, E. W. Rosenberg, J. M. DeStefano, J. Liu, C. Hu, Y. Zhao, Z. Wang, Y. Yao *et al.*, Phys. Rev. X **14**, 031015 (2024).
[40] F. Lieberich, Y. Saito, Y. Agarmani, T. Sasaki, N. Yoneyama, S. M. Winter, M. Lang, and E. Gati, Sci. Adv. **11**, eadz0699 (2025).
[41] C. R. W. Steward, G. Palle, M. Garst, J. Schmalian, and I. Jang, Phys. Rev. B **112**, 064431 (2025).
[42] R. A. Erickson, Phys. Rev. **90**, 779 (1953).
[43] W. Schweika, S. V. Maleyev, T. Brückel, V. P. Plakhty, and L.-P. Regnault, Europhys. Lett. **60**, 446 (2002).
[44] A. S. Borovik-Romanov, Zhur. Eksptl'. i Teoret. Fiz. **38**, 1088 (1960).
[45] J. Baruchel, A. Draperi, M. El Kadiri, G. Fillion, M. Maeder, P. Molho, and J. Porteseil, J. Phys. C **8**, 1895 (1988).
[46] M. Costa and P. Brown, Physica (Amsterdam) **156-157A**, 329 (1989).
[47] Q. Faure, D. Bounoua, V. Balédent, A. Gukasov, V. O. Garlea, A. Ribeiro, J. G. Rau, S. Petit, and P. McClarty, arXiv:2509.07087.
[48] See Supplemental Material at http://link.aps.org/supplemental/10.1103/svrz-315w for details of the theory, the DFT calculations, the experimental setup, and the fitting procedure, which includes Refs. [49–66].

[49] W. O. J. Boo and J. W. Stout, J. Chem. Phys. **65**, 3929 (1976).
[50] H. Ikeda, N. Okamura, K. Kato, and A. Ikushima, J. Phys. C **11**, L231 (1978).
[51] M. Torrent, F. Jollet, F. Bottin, G. Zérah, and X. Gonze, Comput. Mater. Sci. **42**, 337 (2008).
[52] M. A. L. Marques, M. J. T. Oliveira, and T. Burnus, Comput. Phys. Commun. **183**, 2272 (2012).
[53] X. Gonze, F. Jollet, F. Abreu Araujo, D. Adams, B. Amadon, T. Applencourt, C. Audouze, J.-M. Beuken, J. Bieder, A. Bokhanchuk *et al.*, Comput. Phys. Commun. **205**, 106 (2016).
[54] X. Gonze, B. Amadon, G. Antonius, F. Arnardi, L. Baguet, J.-M. Beuken, J. Bieder, F. Bottin, J. Bouchet, E. Bousquet *et al.*, Comput. Phys. Commun. **248**, 107042 (2020).
[55] A. H. Romero, D. C. Allan, B. Amadon, G. Antonius, T. Applencourt, L. Baguet, J. Bieder, F. Bottin, J. Bouchet, E. Bousquet *et al.*, J. Chem. Phys. **152**, 124102 (2020).
[56] F. Jollet, M. Torrent, and N. Holzwarth, Comput. Phys. Commun. **185**, 1246 (2014).
[57] B. Amadon, F. Jollet, and M. Torrent, Phys. Rev. B **77**, 155104 (2008).
[58] M. Verstraete and X. Gonze, Phys. Rev. B **65**, 035111 (2001).
[59] H. M. L. Noad, K. Ishida, Y.-S. Li, E. Gati, V. Stangier, N. Kikugawa, D. A. Sokolov, M. Nicklas, B. Kim, I. I. Mazin *et al.*, Science **382**, 447 (2023).
[60] F. Jerzembeck, H. S. Røising, A. Steppke, H. Rosner, D. A. Sokolov, N. Kikugawa, T. Scaffidi, S. H. Simon, A. P. Mackenzie, and C. W. Hicks, Nat. Commun. **13**, 4596 (2022).
[61] R. L. Melcher, Phys. Rev. B **2**, 733 (1970).
[62] M. S. Ikeda, J. A. W. Straquadine, A. T. Hristov, T. Worasaran, J. C. Palmstrom, M. Sorensen, P. Walmsley, and I. R. Fisher, Rev. Sci. Instrum. **90**, 083902 (2019).
[63] U. Stockert and N. Oeschler, Cryogenics **51**, 154 (2011).
[64] J. A. W. Straquadine, M. S. Ikeda, and I. R. Fisher, Rev. Sci. Instrum. **91**, 083905 (2020).
[65] F. Jerzembeck, Y.-S. Li, G. Palle, Z. Hu, M. Biderang, N. Kikugawa, D. A. Sokolov, S. Ghosh, B. J. Ramshaw, T. Scaffidi *et al.*, Phys. Rev. B **110**, 064514 (2024).
[66] S. Hart and R. W. H. Stevenson, J. Phys. D **5**, 160 (1972).
[67] L. Bartosch, M. de Souza, and M. Lang, Phys. Rev. Lett. **104**, 245701 (2010).
[68] J. Etxebarria, J. M. Perez-Mato, E. S. Tasci, and L. Elcoro, Acta Crystallogr. Sect. A **81**, 317 (2025).
[69] M. E. Barber, A. Steppke, A. P. Mackenzie, and C. W. Hicks, Rev. Sci. Instrum. **90**, 023904 (2019).
[70] X. H. Verbeek, D. Voderholzer, S. Schären, Y. Gachnang, N. A. Spaldin, and S. Bhowal, Phys. Rev. Res. **6**, 043157 (2024).
[71] V. P. Andratskij and A. S. Borovik-Romanov, Sov. Phys. JETP **24**, 687 (1967).
[72] T. Aoyama and K. Ohgushi, Phys. Rev. Mater. **8**, L041402 (2024).
[73] M. S. Ikeda, T. Worasaran, E. W. Rosenberg, J. C. Palmstrom, S. A. Kivelson, and I. R. Fisher, Proc. Natl. Acad. Sci. U.S.A. **118**, e2105911118 (2021).
[74] I. I. Mazin, AAPPS Bull. **35**, 18 (2025).
[75] Y.-M. Wu, Y. Wang, and R. M. Fernandes, Phys. Rev. Lett. **135**, 156001 (2025).
[76] R. Ohlendorf and E. Gati, EDMOND, 10.17617/3.ZLCFJZ (2026).
[77] Y. Shapira, S. Foner, and A. Misetich, Phys. Rev. Lett. **23**, 98 (1969).
[78] M. Komuro, T. Aoyama, and K. Ohgushi, Phys. Rev. B **111**, 214445 (2025).

End Matter

A. Elastocaloric data at different fields and strains—In the following, we present all experimental data of the ECE in MnF_2 as a function of T at different ε_{xy} and $\mu_0 H_z$, that we used to infer the $T^* - T_c^{(0)}$ data in Fig. 1 of the main text. Figure 5 shows η_{xy} of MnF_2 vs T at zero magnetic field and at different compressive strains ε_{xy} up to -0.15%. The data reveal a clear steplike feature around $T \approx 67.5$ K, characteristic for a second-order phase transition, as expected for MnF_2 at zero strain. To better illustrate the strain-induced shift of the transition temperature, the phase transition anomaly is shown on enlarged scales in the inset in Fig. 5. We find that the transition temperature shifts linearly to higher temperatures with increasing compression (see also Fig. S6 in Supplemental Material [48]) and follows $T_c' = T_c^{(0)} + a_1 \varepsilon_{xy}$ with a slope of $a_1 = -59(3)$ K. The ECE jump remains essentially unchanged at different ε_{xy}, as expected for a constant a_1 and a constant specific heat C_ε, following the Ehrenfest relation

$$\frac{\mathrm{d}T_c^{(0)}}{\mathrm{d}\varepsilon_{\mathrm{xy}}} = \frac{\Delta[C_\varepsilon \eta_{xy}]}{\Delta C_\varepsilon}. \tag{A1}$$

Next, we present the ECE at $\mu_0 H_z$ for four selected strain values between -0.04% and -0.15%, as shown in Figs. 6(a)–6(d). For each strain, the ECE feature shifts to lower temperatures with increasing $\mu_0 H_z$ up to 6.44 T, and this suppression is essentially symmetric in field (see Supplemental Material [48]). At zero strain, the field dependence of the critical temperature is well described by $T_c' = T_c^{(0)} + a_2(\mu_0 H_z)^2$ with $a_2 = -0.015\,85(14)$ K/T^2 (see Supplemental Material, Sec. D4 [48]), in excellent agreement with earlier reports of the T-$\mu_0 H_z$ phase diagram [77].

B. Connection to piezomagnetic coefficients—In Ref. [45], the PZM coefficient of MnF_2 was reported as the magnetization induced by stress, σ_{jk}:

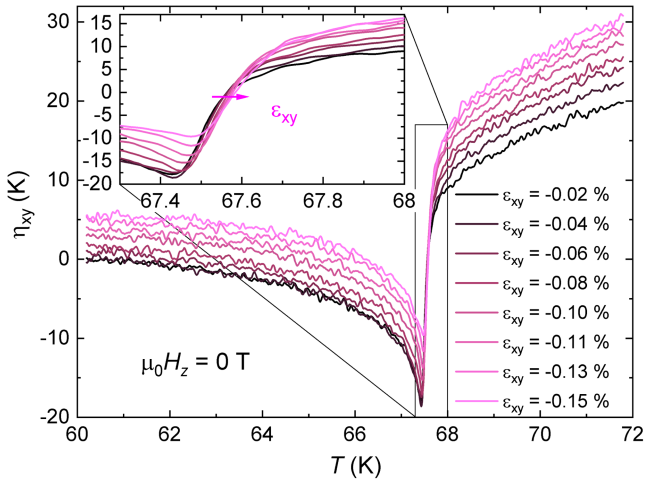

FIG. 5. Elastocaloric effect, $\eta_{xy} = \Delta T/\Delta\varepsilon_{xy}$, of MnF_2 vs temperature T, at different constant strains and zero magnetic field. The inset shows an enlarged view of the data around the phase transition. The pink arrow indicates that the phase transition shifts to higher temperatures with increasing compression (negative strains). The change in the magnitude of the elastocaloric effect at high temperatures likely results from small strain-induced changes of the phononic contributions and is denoted by η_n in the main text.

TABLE I. Literature values of the piezomagnetic coefficient per unit cell of MnF_2 and the corresponding AM coupling constant λ calculated by means of Eq. (B2). Additionally, the temperature at which the piezomagnetic coefficient was measured is stated. Only Λ_{zyx} is allowed by symmetry, whereas Λ_{yzx} is allowed only in the presence of SOC. Λ_{ave} refers to a measurement on a polycrystal.

Λ_{ijk}	λ_{ijk}	T	Ref.
$\Lambda_{zyx} = 5.82e^{-7}$ μB/MPa	0.176	60 K	[45]
$\Lambda_{yzx} = 8.15e^{-7}$ μB/MPa	0.246	20 K	[44]
$\Lambda_{ave} = 1.20e^{-7}$ μB/MPa	0.036	50 K	[78]

$$M_i = \Lambda_{ijk}\sigma_{jk}. \tag{B1}$$

The stress σ_{110} can be connected to the strain ε_{xy} using the appropriate Young's modulus C_0 and the Poisson ratios via $\sigma_{110} = (2C_0/1+\nu)\varepsilon_{xy}$. Together with the definition of the PZM in the main text, this allows us to express λ in terms of the measured Λ:

$$\lambda \approx \frac{\Lambda}{\mu_B \Phi}\frac{2C_0}{1+\nu}. \tag{B2}$$

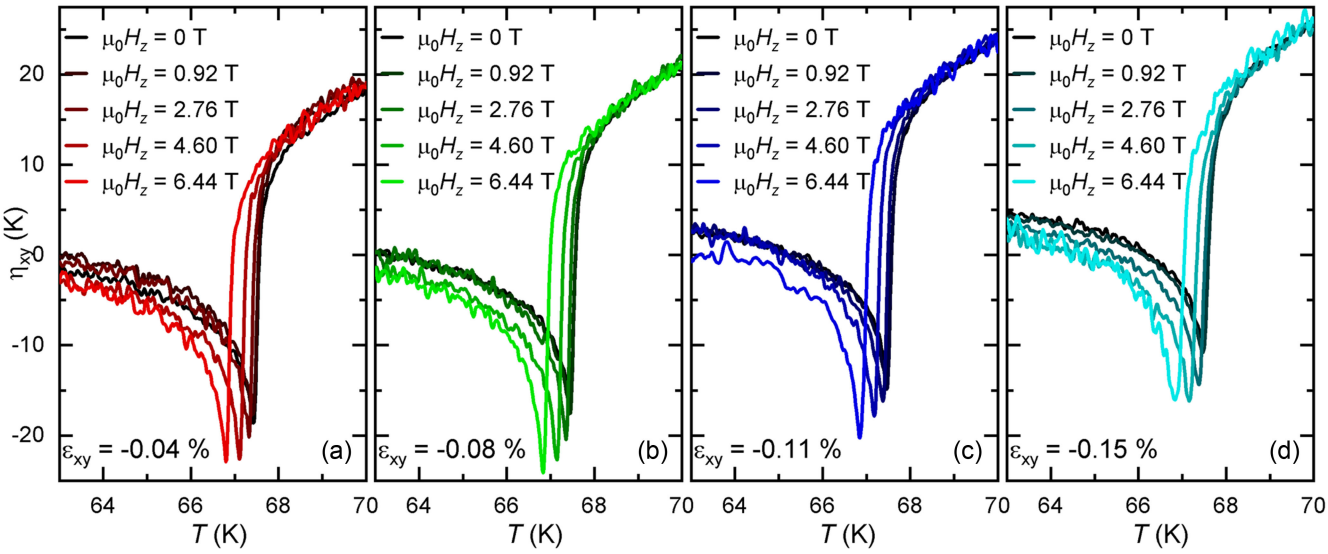

FIG. 6. Elastocaloric effect, $\eta_{xy} = \Delta T/\Delta\varepsilon_{xy}$, of MnF_2 vs temperature T, taken at constant strains [(a) $\varepsilon_{xy} = -0.04\%$, (b) $\varepsilon_{xy} = -0.08\%$, (c) $\varepsilon_{xy} = -0.11\%$, and (d) $\varepsilon_{xy} = -0.15\%$] at different magnetic fields (0–6.44 T).

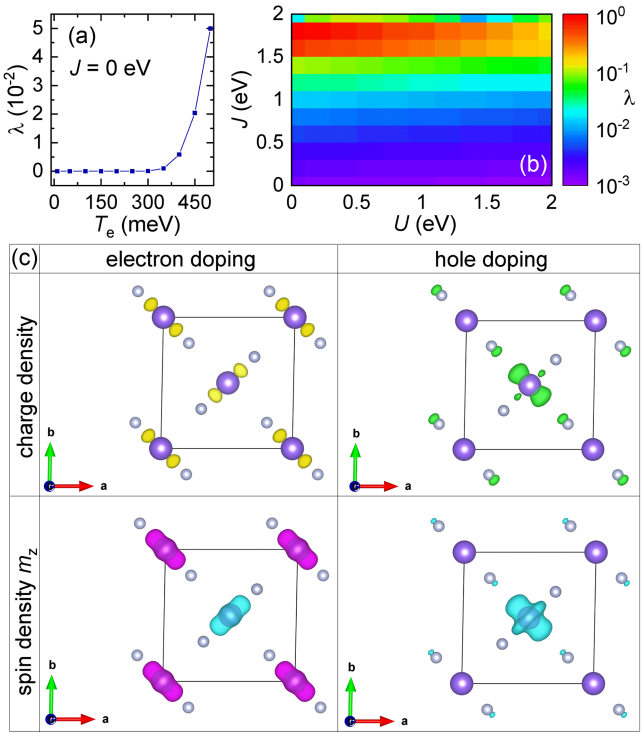

FIG. 7. (a) Calculated λ as a function of electronic temperature, extracted from calculations of the piezomagnetism through DFT calculations of fully stoichiometric MnF_2. For large enough electronic temperatures that give rise to considerable number of electron-hole pairs to be excited, λ is strongly enhanced. (b) When an on-site $+U$ correction is introduced in the DFT calculations, λ shows a minor dependence on the value of U used but a stronger dependence on the Hund's coupling J. Nevertheless, physically meaningful values of J do not lead to large enough λ values that agree with the experimental observations. (c) Isosurfaces of the doping-induced changes in the charge densities (green, positive change; yellow, negative change) and spin densities (pink, positive change; cyan, negative change) under electron and hole doping, shown around the Mn ions (purple) and F ions (gray).

In Table I, we list the previously reported value of Λ_{zyx}, which is the PZM coefficient allowed by symmetry only, as well as the one of Λ_{yxz}, which is allowed only in the presence of SOC, as well as the corresponding λ_{ijk} values using the assumption that $\Phi \approx 1$. This assumption is likely violated, especially near $T_c^{(0)}$ where Φ becomes small, leading to an underestimation of λ according to Eq. (B2).

The DFT-based calculation results for λ of pristine MnF_2 are shown in Figs. 7(a) and 7(b) as a function of the electronic temperature T_e for $J = 0$ eV (a) and as a function of J and U at $T = 0$ K (b). In addition, Fig. 7 (c) shows the change in the charge and spin densities upon electron and hole doping, respectively (see the main text, Fig. 4).